

## High-resolution wave-equation AVA imaging: Algorithm and tests with a data set from the Western Canadian Sedimentary Basin

Juefu Wang<sup>1</sup>, Henning Kuehl<sup>2</sup>, and Mauricio D. Sacchi<sup>1</sup>

### ABSTRACT

This paper presents a 3D least-squares wave-equation migration method that yields regularized common-image gathers (CIGs) for amplitude-versus-angle (AVA) analysis. In least-squares migration, we pose seismic imaging as a linear inverse problem; this provides at least two advantages. First, we are able to incorporate model-space weighting operators that improve the amplitude fidelity of CIGs. Second, the influence of improperly sampled data (footprint noise) can be diminished by incorporating data-space weighting operators. To investigate the viability of this class of methods for oil and gas exploration, we test the algorithm with a real-data example from the Western Canadian Sedimentary Basin.

To make our problem computationally feasible, we utilize the 3D common-azimuth approximation in the migration algorithm. The inversion algorithm uses the method of conjugate gradients with the addition of a ray-parameter-dependent smoothing constraint that minimizes sampling and aperture artifacts. We show that more robust AVA attributes can be obtained by properly selecting the model and data-space regularization operators. The algorithm is implemented in conjunction with a preconditioning strategy to accelerate convergence.

Posing the migration problem as an inverse problem leads to enhanced event continuity in CIGs and, hence, more reliable AVA estimates. The vertical resolution of the inverted image also improves as a consequence of increased coherence in CIGs and, in addition, by implicitly introducing migration deconvolution in the inversion.

### INTRODUCTION

The reliable inversion of prestack seismic data is an important step toward a robust and accurate estimate of physical rock properties and fluid indicators, the ultimate goal of quantitative seismic interpretation. In this context, common image gathers (CIGs) can yield valuable, reflection-angle-dependent amplitude information. Conventionally, CIGs are generated as a function of offset and are then converted to angle in a subsequent step. Alternatively, imaging in the reflection angle (Stolt and Weglein, 1985) or local ray-parameter domain (de Bruin et al., 1990) directly yields amplitude variations versus angle (AVA) or amplitude variations versus ray parameter (AVP), respectively. The latter can be converted from ray parameter to angle by simple scaling, taking the reflector dip and the migration velocity into account (see Appendix A).

In recent years, numerous papers have addressed the theoretical and computational aspects of angle and ray-parameter imaging for Kirchhoff migration and wave-equation migration (e.g., Xu et al., 1998; Prucha et al., 1999; Wapenaar et al., 1999; Mosher and Foster, 2000; Sava et al., 2001). At the same time, in an effort to improve conventional migration, Nemeth et al. (1999) and Duquet et al. (2000) have developed schemes for least-squares migration based on Kirchhoff modeling/migration operators to mitigate artifacts caused by data aliasing, acquisition footprint, and illumination issues. Kuehl and Sacchi (2002, 2003) combine both developments and show that regularized least-squares wave-equation migration can reduce aliasing in ray-parameter image gathers, leading to more robust AVA estimates. They propose a formulation of the least-squares migration problem in terms of double-square-root (DSR) phase-shift propagators.

In this article, we present the 3D extension of the 2D inversion algorithm described in Kuehl and Sacchi (2002). We use the common-azimuth operator developed by Biondi and Palacharla (1996) combined with a split-step correction for

Manuscript received by the Editor May 27, 2004; revised manuscript received November 29, 2004; published online September 9, 2005.

<sup>1</sup>University of Alberta, Department of Physics, Avadh Bhatia Physics Laboratory, Edmonton, Alberta T6G 2J1, Canada. E-mail: jwang@phys.ualberta.ca; sacchi@phys.ualberta.ca.

<sup>2</sup>Formerly University of Alberta, Department of Physics, Edmonton, Alberta, Canada; presently Shell Canada Ltd., P.O. Box 100, Station M, Calgary, Alberta T2P 2H5, Canada. E-mail: henning.kuehl@shell.com.

© 2005 Society of Exploration Geophysicists. All rights reserved.

lateral velocity variations (Popovici, 1996). When the macrovelocity field has strong variations, we enhance the operator accuracy with the phase-shift-plus-interpolation (PSPI) technique (Gazdag and Sguazzero, 1984). Common-azimuth migration results in significant computational cost savings. To further reduce the turnaround time, we adopt a preconditioning strategy that follows the work on 2D least-squares migration by Prucha et al. (2002). An efficient algorithm is crucial if least-squares migration is to be applied to data volumes of realistic size. In any case, costly least-squares migration is not a feasible method for several iterations of velocity analysis. The least-squares migration approach is therefore intended to improve the seismic image after a reasonably good velocity field has been derived.

As an example, we apply least-squares migration to a 3D data set from the Western Canadian Sedimentary Basin. A comparison with borehole-derived synthetics and theoretical AVA supports the case for regularized imaging methods in situations where subtle stratigraphic features and fluid effects need to be resolved.

### REGULARIZED LEAST-SQUARES, 3D WAVE-EQUATION MIGRATION

Consider seismic data as the result of a linear transformation on an earth model  $\mathbf{m}$ :

$$\mathbf{d} = \mathbf{L}\mathbf{m} + \mathbf{n}, \quad (1)$$

where  $\mathbf{d}$  denotes the preprocessed data;  $\mathbf{L}$  is the forward operator;  $\mathbf{m}$  is the earth model, a set of ray-parameter-dependent CIGs; and  $\mathbf{n}$  denotes additive noise. Conventional migration entails applying  $\mathbf{L}'$ , the adjoint of  $\mathbf{L}$ , to the observed data. The adjoint operator  $\mathbf{L}'$  can be decomposed into two steps: wavefield extrapolation and ray-parameter imaging (see Appendix A for more details). The second step amounts to a change of variables by a radial-trace transform, which introduces a transformation Jacobian (Sava et al., 2001). When the data are properly sampled, the amplitude in the CIG can be corrected by applying an approximate inverse of the imaging Jacobian.

The Jacobian weighting attempts to make the adjoint operator behave like the inverse. However, this correction is not sufficient to achieve good amplitude fidelity in situations where the image is corrupted by aliasing artifacts introduced by inadequate spatial sampling. These artifacts can be alleviated, however, by constraining the solution to exhibit a certain degree of smoothness along the ray-parameter axis. Here, we adopt a cost function  $F$  [similar to the cost function introduced by Ehinger and Lailly (1991)] to retrieve a least-squares migrated image that fits the observations and also exhibits

smoothness or continuity along the ray-parameter axis:

$$F(\mathbf{m}) = \|\mathbf{W}(\mathbf{d} - \mathbf{L}\mathbf{m})\|^2 + \lambda^2 \|\mathbf{D}_{1hx}\mathbf{m}\|^2, \quad (2)$$

where  $\mathbf{W}$  is a diagonal weighting matrix (data-space weighting) used to decrease the influence of missing observations in the migrated image. The diagonal elements of  $\mathbf{W}$  consist of zeroes and ones, weighting dead traces and live traces, respectively. The regularization operator  $\mathbf{D}_{1hx}$  (model-space weighting) is a first-order derivative operator along the inline ray-parameter direction. In regularized least-squares migration (RLSM), we seek a model  $\mathbf{m}$  by minimizing the sum of the two norms where the trade-off parameter  $\lambda$  determines the amount of smoothness. We minimize the objective function using a conjugate-gradients (CG) algorithm (Hestenes and Stiefel, 1952). Hence, the algorithm reduces to the sequential application of the following operators: migration  $\mathbf{L}'$ , demigration  $\mathbf{L}$ , unsmoothing  $\mathbf{D}_{1hx}$ , and the adjoint of unsmoothing  $\mathbf{D}'_{1hx}$ . The operator  $\mathbf{D}_{1hx}$  is a discrete derivative (high-pass filter), and the transpose operator  $\mathbf{D}'_{1hx}$  is a discrete anticausal derivative (Claerbout, 2004). The construction of the modeling and regularization operators and their adjoints is described by Kuehl (2003). In this paper, we replace the 2D wave extrapolator by a 3D common-azimuth extrapolator (Biondi and Palacharla, 1996).

The choice of trade-off parameter  $\lambda$  can pose a challenge for a large-scale linear problem such as regularized least-squares migration. Obviously, it is not feasible to determine  $\lambda$  from a trade-off curve [L-curve method, Hansen (1998)]. In practice, we therefore iterate the following procedure until a good value for  $\lambda$  is found. We run least-squares migration for a couple of iterations for only a few frequencies, starting with a small trade-off parameter — for example,  $\lambda = 0.0001$  — and monitor the data misfit of a few common-midpoint (CMP) gathers. If, within the first two iterations, the data residual norm reduces to 30% to 60% of the input data norm, the trade-off parameter is accepted. If the fit is poor, we decrease the trade-off parameter by 1/10. Conversely, if we are overfitting the data, we increase  $\lambda$  by a factor of 10.

### Synthetic data example

We created a simple 2D acoustic data set using a ray tracer that accounts for the correct reflector AVA, cylindrical divergence (line sources), and interface transmission losses in a laterally invariant earth model. The data were then copied to a number of inlines to simulate 3D common-azimuth data generated by line sources. The model consists of four flat layers and a half-space. Table 1 describes the model in terms of velocity and density. Note that cylindrical divergence is in agreement with the assumptions made for the common-azimuth migration operator (Biondi and Palacharla, 1996). When dealing with real data, we approximately transform point sources to line sources by multiplying the data by the square root of the two-way traveltimes.

Each CMP gather has 61 offsets with a spacing of 25 m. The data set consists of 10 inlines, each of which has 10 CMP gathers. Both inline and crossline CMP spacings are 25 m. Finally, we randomly remove 70% of the traces to simulate a very sparse 3D survey.

**Table 1. Model parameters for the 3D synthetic data.**

Velocity (m/s)	Density (g/cm <sup>3</sup> )	Thickness (m)
2000	2.25	500
2350	1.6	300
1900	2.3	300
2500	1.7	300
2500	2.0	Half-space

Figure 1 illustrates the capability of RLSM to reconstruct 3D seismic data. Figure 1a displays four CMP gathers of the original data, and Figure 1b shows the reconstructed CMP gathers after 15 CG iterations. The residuals (Figure 1c) are insignificant. This is a reassuring, albeit expected, result. Obviously, successful data reconstruction prior to conventional migration would be a more efficient alternative to least-squares migration in this case. Many schemes for wavefield reconstruction have been proposed and successfully applied. For example, Liu et al. (2003) have devised a Fourier reconstruction method that can deal with sparse data similar to the example shown in this section. However, the purpose of this study is to glean the benefits of least-squares migration without resorting to other processing techniques. This is not strictly of academic interest, since least-squares migration promises to achieve benefits beyond data reconstruction. Hu et al. (2001) demonstrate that migration deconvolution, implicitly accounted for in least-squares migration, can help to sharpen the seismic image by deconvolving the migration point-spread function. The point-spread function results from the band-limited nature of the imaging process and tends to blur the seismic image. In our real-data example, least-squares migration generates a higher-resolution image than conventional migration, which agrees with the assertion made by Hu et al. (2001).

Figure 2 compares CIGs (at the same spatial location) computed via migration, RLSM after four CG iterations, and RLSM after 15 iterations. With more CG iterations, the coherency of the CIG is gradually improved and aliasing arti-

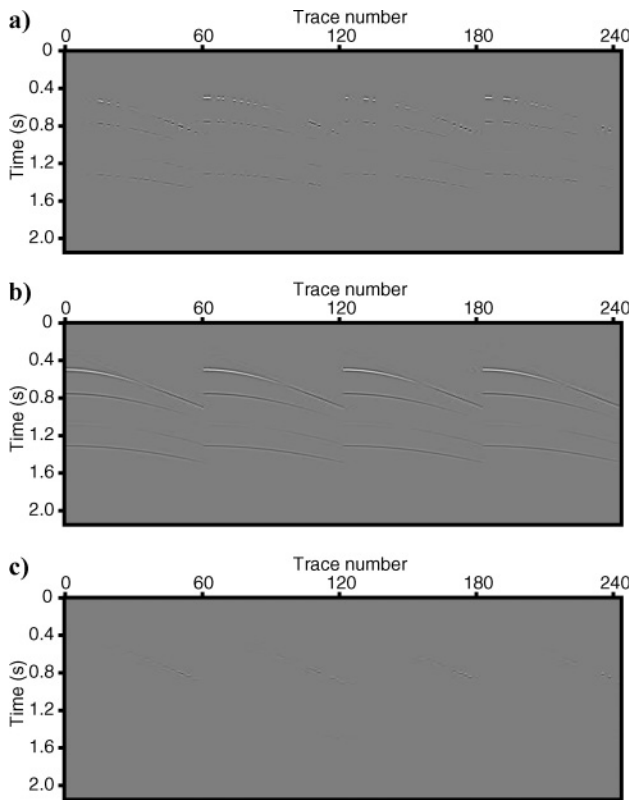


Figure 1. Comparison between observed and reconstructed data. (a) Four neighboring CMP gathers. Each gather has 61 offsets with 25-m spacing. (b) Reconstructed CMP gathers after 15 CG iterations. (c) Difference between the original live traces and the corresponding reconstructions.

facts are further mitigated. Notice the limited aperture effect in the migration result, manifesting itself as spurious tails. Part of the problem lies in the fact that the highest invertible, full-bandwidth ray parameter is determined by the upper limit of the offset wavenumber. Going beyond this limit in the radial-trace transform reduces the wavelet bandwidth. This is particularly obvious for the first event in our example. One has to be aware of this, and muting the CIGs at the upper ray-parameter limit may be advisable. However, suppression of this effect would be preferable. Refer to Sava and Fomel (2003) for a more detailed discussion on angle- and ray-parameter-domain imaging.

Figure 3 compares the extracted AVA curves of the four events by two different methods. The top panel shows the migration (with the imaging Jacobian correction applied), and the bottom panel shows the RLSM result. For better comparison, the smoothed migrated AVA curves are also shown in the top row. The migrated amplitudes are obviously distorted by missing data. On the other hand, RLSM retrieves the AVA closely within the invertible angle range. Kuehl (2003) finds that least-squares migration is also beneficial in the presence of white noise, despite an expected degradation of amplitude

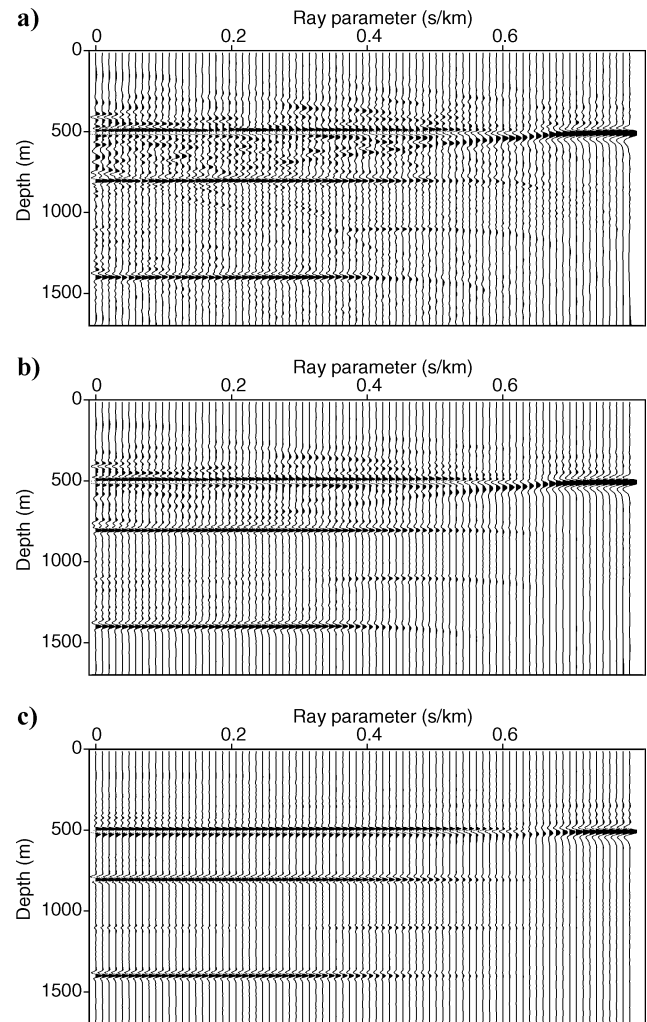


Figure 2. CIGs with varying CG iterations. (a) CIG after migration. (b) CIG after four CG iterations. (c) CIG after fifteen CG iterations.

fidelity with decreasing signal-to-noise (S/N) ratio. Notice that the effect of the imaging Jacobian is inherent in the inversion.

Figure 4 shows the relationship between the normalized data residual norm and CG iteration. The misfit flattens out after 15 iterations; more iterations do not significantly impact the AVA estimate.

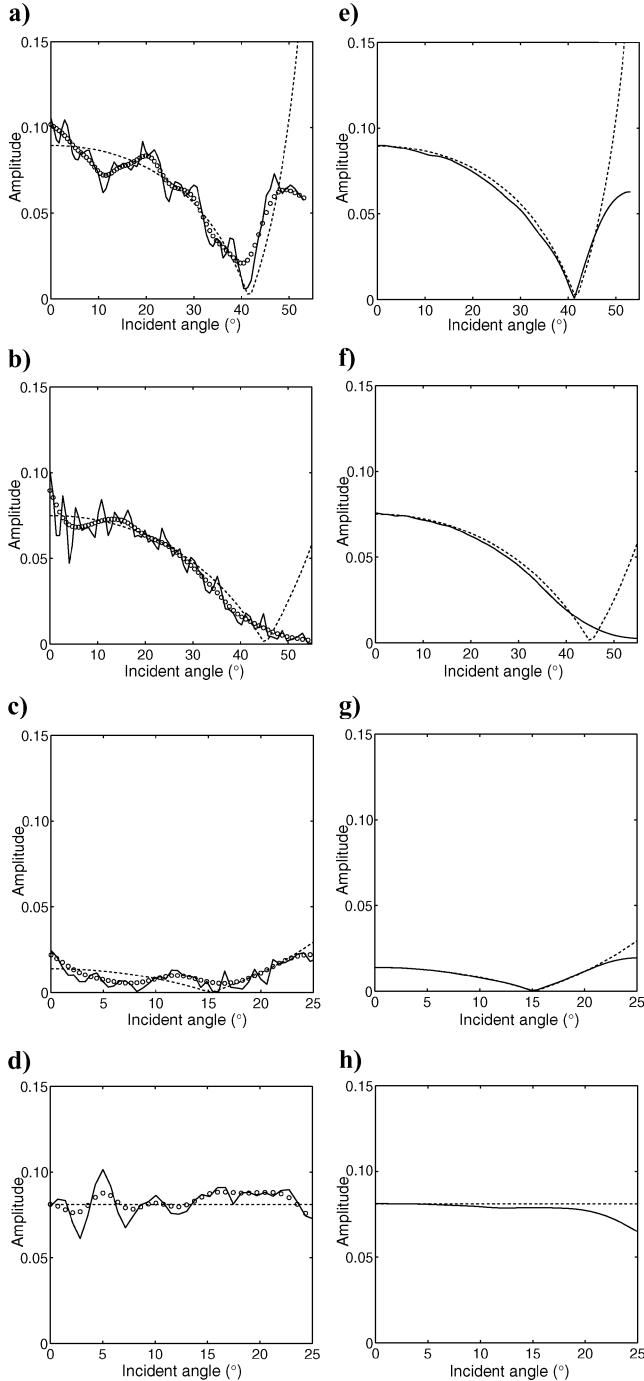


Figure 3. Extracted AVA curves produced by migration for the events at depths (a) 500 m, (b) 800 m, (c) 1100 m, and (d) 1400 m. The dashed lines are the theoretical AVA, the solid lines are the migration result, and the circled lines are the smoothed migration result (Hamming filtered). (e)–(h) Extracted AVA curves produced by RLSM (15 iterations). The solid lines are the RLSM-inverted AVA.

### Preconditioned implementation of RLSM

A negative aspect of RLSM is its computational cost. Each CG iteration requires one full migration/demigration sequence, which clearly limits RLSM in industrial applications.

Preconditioning strategies for semi-iterative solvers can help to speed up convergence and have been studied extensively in applied mathematics (Saad, 1991; Hanke and Hansen, 1993). Indeed, preconditioning schemes have been applied successfully in prestack imaging by coupled linearized inversion (Ehinger and Lailly, 1991), wave-equation least-squares migration (Prucha and Biondi, 2002), interpolation problems (Fomel and Claerbout, 2003), and Radon processing (Trad et al., 2003). In our implementation, equation 2 is solved with a simple change of variable:

$$\mathbf{z} = \mathbf{D}_{1hx} \mathbf{m}. \quad (3)$$

Substituting  $\mathbf{m}$  in equation 2 leads to

$$\begin{aligned} F(\mathbf{z}) &= \|\mathbf{W}(\mathbf{d} - \mathbf{L}\mathbf{P}\mathbf{z})\|^2 + \lambda^2 \|\mathbf{z}\|^2 \\ &\equiv \|\mathbf{W}(\mathbf{d} - \tilde{\mathbf{L}}\mathbf{z})\|^2 + \lambda^2 \|\mathbf{z}\|^2, \end{aligned} \quad (4)$$

where  $\mathbf{P}$ , in theory, is the inverse of  $\mathbf{D}_{1hx}$ . Here, rather than inverting  $\mathbf{D}_{1hx}$ , we replace  $\mathbf{P}$  by an operator that behaves similarly as the inverse of  $\mathbf{D}_{1hx}$ . If  $\mathbf{D}_{1hx}$  is a discrete operator, we can think of it as a high-pass operator or filter. Therefore,  $\mathbf{P}$  must be a low-pass operator. In our implementation, to apply  $\mathbf{P}$  is equivalent to applying a 1D low-pass filter (Hamming window) to the image gathers. The convolution, in this context, is used to remove artifacts arising from incomplete sampling, additive noise in the original data, and operator artifacts (Kuehl and Sacchi, 2003).

The new cost function is similar but not identical to equation 3 since  $\mathbf{P}$  is not exactly equivalent to the inverse of  $\mathbf{D}_{1hx}$ . However, the solutions are expected to be of similar character and quality. Indeed, our tests confirm that both techniques yield almost indistinguishable results, but the preconditioned solution is reached significantly faster.

Mathematically, the logic behind this step is that a good preconditioner will change the distribution of eigenvalues of the operator  $\mathbf{L}'\mathbf{L}$  (Saad, 1991). Proper preconditioning will

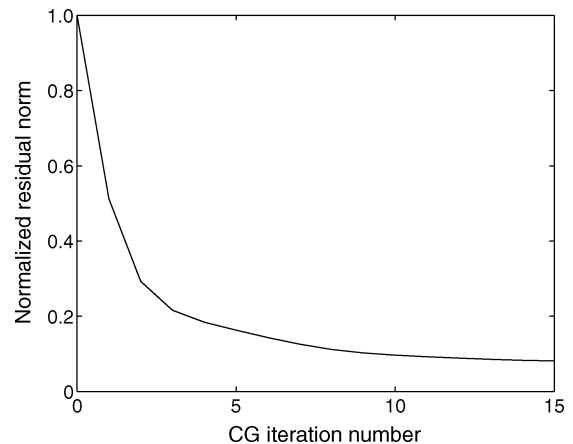


Figure 4. Normalized residual norm  $\|\mathbf{W}(\mathbf{L}\mathbf{m} - \mathbf{d})\|^2$  versus CG iteration.

introduce clustering of large eigenvalues; consequently, the CG method will require fewer iterations to minimize the cost function  $F$ . Although we have no formal proof of this, we found that a low-pass filter as the preconditioner provides a good solution within only a few CG iterations of least-squares migration. Our preconditioning strategy is similar to the good-pass operator used by Ronen et al. (1995) for dealiasing the dip-moveout operator. Here, the good-pass operator is the Hamming smoothing window and the bad-pass operator is the first-order derivative.

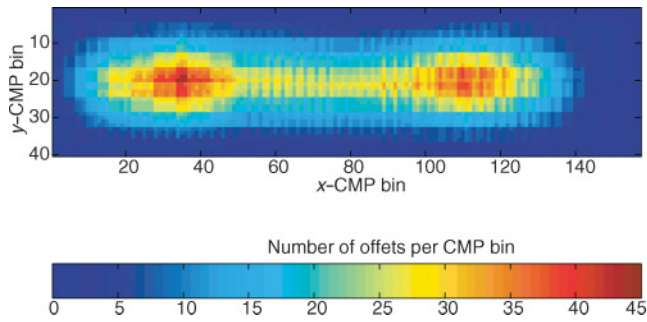


Figure 5. Offset distribution per CMP bin for the Erskine data set, Western Canadian Sedimentary Basin. The number of offsets in each bin is color coded.

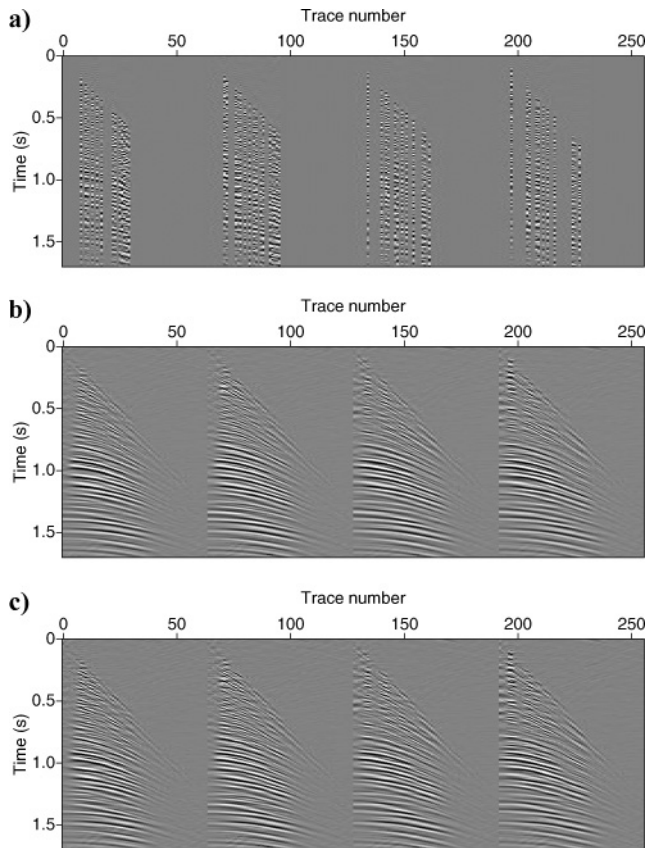


Figure 6. Comparison between observed and reconstructed data at inline 10. (a) Original CMP gathers. (b) Reconstructed CMP gathers after eleven CG iterations. (c) Reconstructed CMP gathers after four preconditioned CG iterations.

Furthermore, preconditioned least-squares migration allows us to set the trade-off parameter  $\lambda$  to zero and let the number of CG iterations control the data fitting (Hanke and Hansen, 1993). This saves time otherwise required for finding a proper trade-off parameter.

**FIELD DATA EXAMPLE**

We compare the performance of migration, RLSM, and preconditioned RLSM using the Erskine data set acquired in southern Alberta, Canada. The small 3D survey targets the Leduc reef, a carbonate play in the Western Canadian Sedimentary Basin. The data were first binned, and a constant common-azimuth subset was extracted. The binned data consist of 157 inlines and 40 crosslines. The offset ranges from 75 to 3000 m, with a highly uneven and sparse distribution (Figure 5).

Figure 6a shows four adjacent CMP gathers extracted from inline 10. Forward modeling, after inversion, is used to recover the data on the complete input grid. The resulting reconstructed gathers are depicted in Figure 6b (RLSM) and c (preconditioned RLSM).

Figure 7 shows the CIGs with offset ray parameters ranging from 0 to 800  $\mu\text{s/m}$  and with an interval of 6.25  $\mu\text{s/m}$  at inline

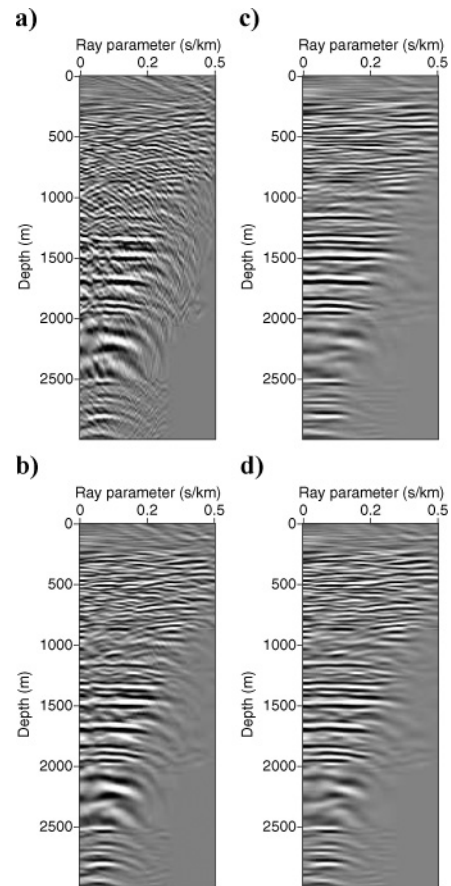


Figure 7. CIGs at crossline 10, inline 71. (a) CIG produced by migration. (b) CIG after four CG iterations. (c) CIG after eleven CG iterations. (d) CIG after four preconditioned CG iterations.

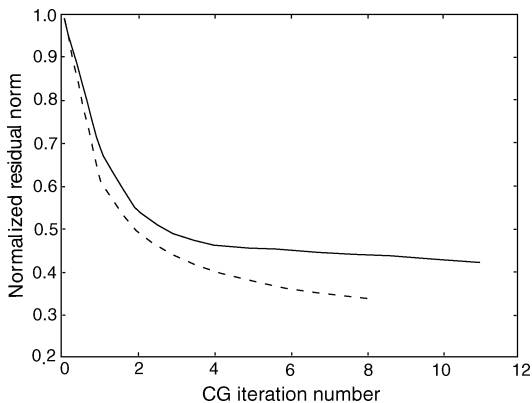


Figure 8. Normalized residual norm  $\|\mathbf{W}(\mathbf{Lm} - \mathbf{d})\|^2$  versus CG iteration. Dashed curve — preconditioned CG. Solid curve — CG.

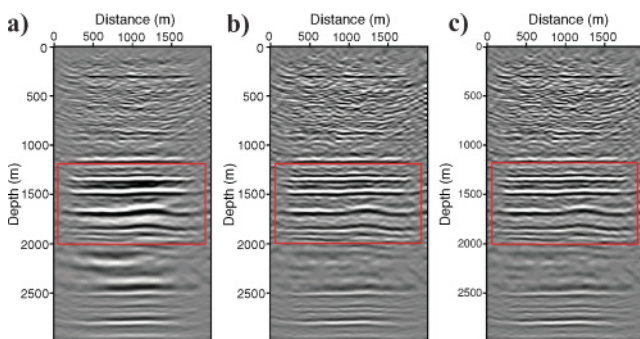


Figure 9. Stack of inline 71. (a) Stack produced by migration. (b) Regularized least-squares migration (eleven iterations). (c) Preconditioned regularized least-squares migration (four iterations). The highlighted areas are enlarged in Figure 10.

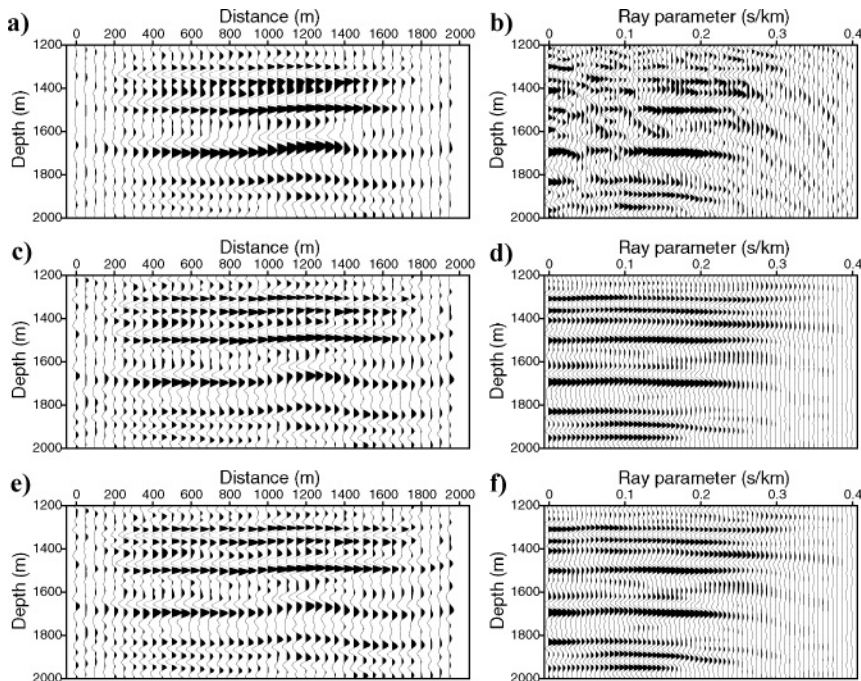


Figure 10. Detailed image of inline 71 with CIG at crossline 10. (a) Stack after migration. (b) CIG corresponding to (a). (c) Stack after eleven CG iterations. (d) CIG corresponding to (c). (e) Stack after four preconditioned CG iterations. (f) CIG corresponding to (e).

71 and crossline 10. The maximum ray parameter is  $500 \mu\text{s}/\text{m}$ . Figure 7a portrays the migrated CIG with obvious aliasing artifacts, and Figure 7b and c depict the least-squares inverted CIG after four and eleven iterations, respectively. Figure 7d shows the result of preconditioned RLSM after only four iterations with a quality similar to that of Figure 7c. The evolution of the normalized residual norm,  $\|\mathbf{W}(\mathbf{Lm} - \mathbf{d})\|^2$ , versus CG iteration can be seen in Figure 8. As expected, the preconditioned RLSM converges faster than RLSM with no preconditioning.

In general, to limit the computational cost of the inversion, we stop the CG algorithm before complete convergence. We monitor a small subset of the reconstructed data (see Figure 6) to control the degree of fitting. This is important since overfitting leads to artifacts. Conversely, underfitting leads to incomplete recovery of the missing observations.

The structural image is computed by stacking the CIGs. The stacked images obtained with migration, the least-squares migration stack, and the preconditioned least-squares migrated stack are displayed in Figure 9. Both RLSM and preconditioned RLSM lead to better reflector continuity in low-fold areas.

Figure 10a, c, and e show details of the stacks displayed in Figure 9 and their associated CIGs (Figure 10b, d, and f) at crossline 10. Note the considerably improved resolution. This effect can be explained as follows: First, by imposing smoothness on the inverted CIG, individual traces stack more coherently. In particular, part of the smearing produced by the aperture limitation (nonflatness at high ray parameters) is attenuated; therefore, the stacked CIG better preserves the high frequencies. Second, as mentioned earlier, least-squares migration automatically accounts for migration deconvolution described by Hu et al. (2001), which helps to sharpen the image. This is an important concept that can lead to higher resolution.

It is conceivable that adding a vertical sparseness constraint could further increase the vertical resolution. The deconvolution effect is also visible in Figure 11, where we compare stacked images at crossline 24.

For better performance assessment, we generated a synthetic CIG based on available sonic-log data from a well located at inline 76 and crossline 24. A second well, located outside the survey area, had density- and sonic-log information. Correlation of the two sonic logs allowed us to match the density log to the log located within the survey. This relatively crude approach appears to be justified, since the sonic logs agree very well (Figure 12). The shear-wave velocities are assumed to follow Castagna's mudrock regression  $V_s = (V_p - 1360 \text{ m/s})/1.16$  (Castagna et al., 1985). Since Castagna's formula is not valid for carbonates, we restrict the AVA analysis to the Ellerslie Formation (sandstone) and the Banff Formation (shale) (see Figure 13) as indicated in the stratigraphic column (Mossop and Shetsen, 1994). Unfortunately, by disregarding the deeper carbonates, we exclude the Leduc reef, which is the actual exploration target. However, this way we do not introduce

further uncertainties by attempting to estimate the carbonate shear-wave velocities. With the compressional-wave velocities, estimated shear-wave velocities, and the calibrated densities, we calculate the angle-dependent reflectivity traces using the Aki and Richards approximation of Zoeppritz's equations (Aki and Richards, 1980).

The inverted CIG at the well location is displayed in Figure 14. Figure 15 compares the time-converted Aki and

Richards synthetic CIG and the time-converted CIG in more detail. Given the degree of uncertainty associated with the synthetic CIG and the sparseness of the field data, the match is acceptable, despite some discrepancies. The picked AVA for the prominent Ellerslie/Banff event at 0.7 s in Figure 16 fits the synthetic AVA well within 12° to 27°. Outside this angle range, the lack of offset data makes a reliable AVA estimate impossible.

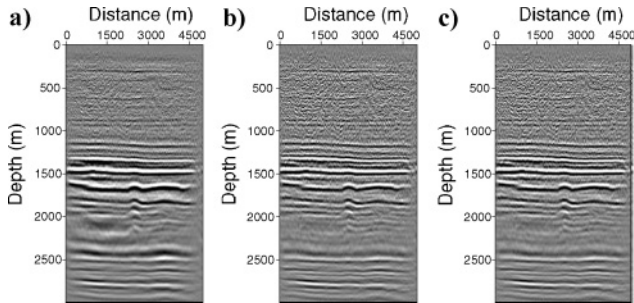


Figure 11. Stack of crossline 24. (a) Migration. (b) Least-squares migration after eleven CG iterations. (c) Preconditioned least-squares migration after four iterations.

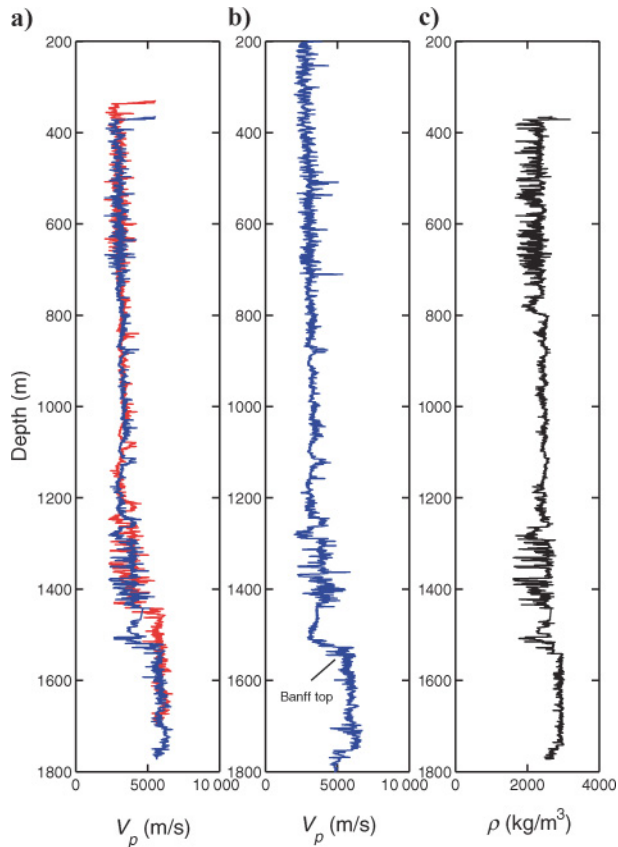


Figure 12. Depth correlation of log traces. (a) Sonic log trace  $V_p$  outside the survey area. The red curve is the trace at the original depth. The blue curve is the same trace with depth calibrated to the local trace shown in (b). (b) Sonic-log trace at inline 76, crossline 24. (c) Density-log trace outside the survey area. The depth has been adjusted to match the sonic-log trace within the survey area.

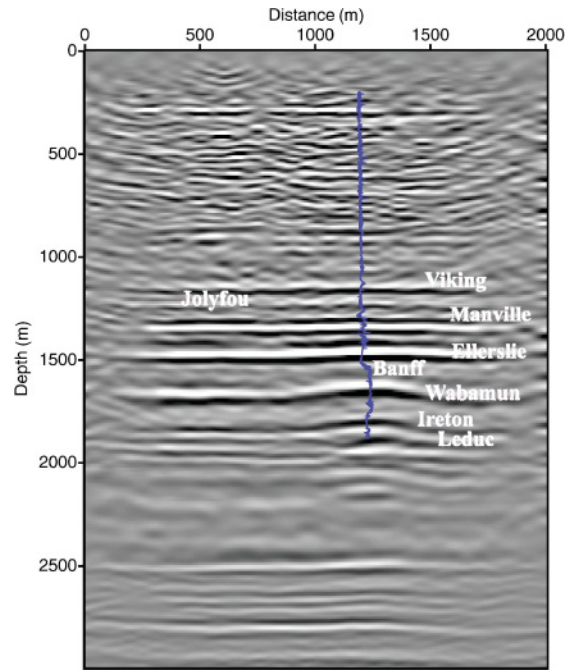


Figure 13. Strata correlation for the survey area of the Erskine data set. The background is the stack of inline 76; the blue curve is the local sonic log (same as Figure 12b). The stack and the sonic log correlate relatively well.

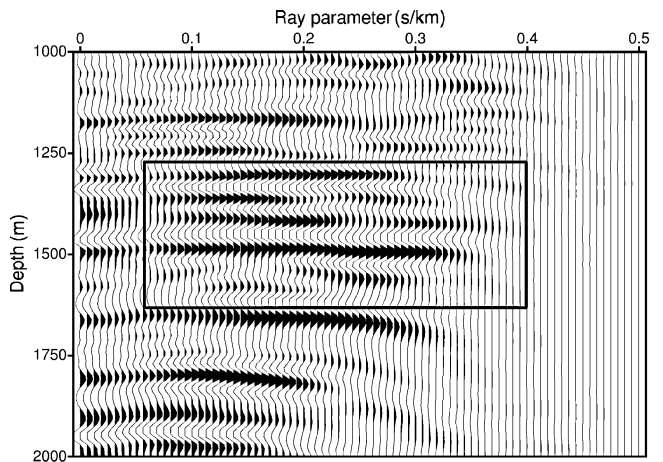


Figure 14. CIG at inline 76, crossline 24. See Figure 15b for the AVA and time conversion of the highlighted area.

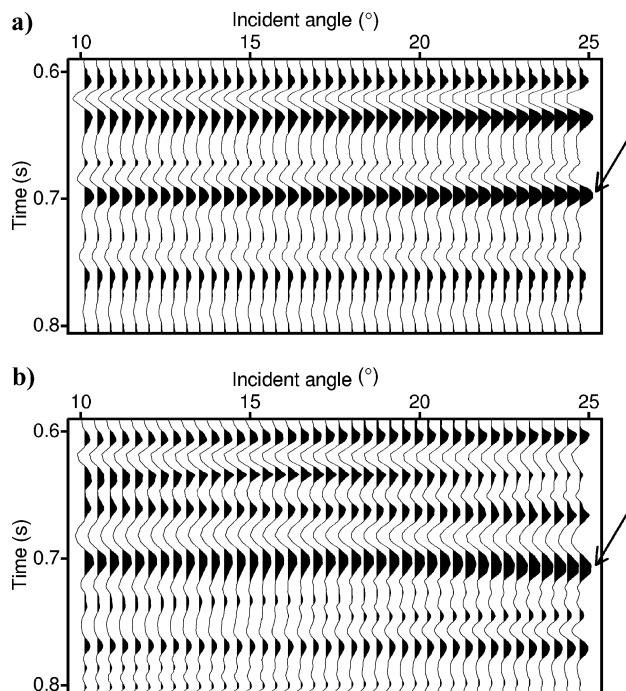


Figure 15. Comparison between (a) the synthetic CIG and (b) the inverted CIG. Both CIGs are displayed in the time domain. The arrows point out the event at depth 1500 m. AVA curves for this event are shown in Figure 16. Since the events are quite flat, AVA is calculated from AVP using equation A-5 with a zero inline dip angle.

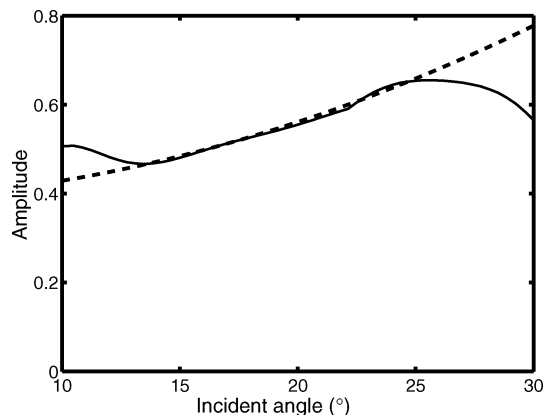


Figure 16. Comparison between the synthetic AVA and the inverted AVA. Dashed curve — synthetic AVA for the event at depth 1500 m. Solid curve — inverted AVA for the same event (see Figure 15).

## DISCUSSION AND CONCLUSIONS

Good-quality CIGs are key for amplitude-supported seismic interpretation aimed at estimating rock and fluid properties. Our field-data test supports the assertion that regularized least-squares migration improves amplitude robustness and image resolution, even when the data are very sparse and aliasing hampers the AVA analysis. The preconditioned implementation of regularized least-squares migration cuts the computational cost significantly, so that an industry applica-

tion of least-squares migration can be considered. Each CG iteration involves one migration/modeling sequence. In our tests, we found good convergence can be achieved within four iterations of preconditioned RLSM, which is a cost equivalent to eight conventional migrations. This is a dramatic improvement over regularized least-squares migration, with a cost equivalent to about 20 migrations.

Clearly, computationally less-demanding techniques, such as interpolation prior to migration, attempt to address the data issues discussed in this paper. Hence, to better appreciate the added benefits of least-squares migration, a careful comparative study between more conventional processing and least-squares migration is in order.

In spite of this caveat, least-squares migration deserves special attention as it is the unifying link between imaging and inversion. It allows us to fit the seismic data and, at the same time, impose geophysically sensible constraints on the seismic model. We expect that other regularization schemes will be proposed in the future. For instance, an inversion for CIGs that are parameterized in terms of AVA intercept and gradient combined with a spatial smoothness constraint that conforms to the geological structure may be one avenue to develop least-squares migration further.

## ACKNOWLEDGMENTS

The Signal Analysis and Imaging Group at the University of Alberta acknowledges financial support from the following companies: GeoX Ltd., EnCana Ltd., Veritas GeoServices, and the Schlumberger Foundation. This research has also been supported by the National Sciences and Engineering Research Council of Canada and the Alberta Department of Energy. We thank Brian Russel, Harald Huebscher, and Dean Rokosh for providing the WCSB log data and for helpful discussions. We also acknowledge reviewers S. Fomel, G. Palacharla, B. Duquet, and W. Schneider Jr., for their valuable suggestions on improving the paper.

## APPENDIX A

### IMAGING 3D COMMON-AZIMUTH DATA

AVA imaging of 3D common-azimuth data can be described as linking wavefield propagation, AVP imaging, and AVP to AVA conversion. The surface wavefield is downward continued in the earth by a phase-shift operator. At each depth, AVP image gathers are produced by a radial-trace transform. Finally, the AVP image gathers are converted to angle by scaling the AVA gathers. This appendix lists the formulas involved in wavefield propagation and imaging.

For computational efficiency, we adopt Biondi and Palacharla's common-azimuth phase-shift operator to propagate the wavefield in the frequency domain  $\omega$  (Biondi and Palacharla, 1996):

$$P(z + dz, \omega, k_{mx}, k_{my}, k_{hx}) = P(z, \omega, k_{mx}, k_{my}, k_{hx}) \times e^{-ik_z dz}, \quad (\text{A-1})$$

where the vertical wavenumber  $k_z$  is calculated by a modified DSR equation:

$$k_z = \omega \left( \sqrt{\frac{1}{v(\mathbf{r}, z)^2} - \frac{1}{4\omega^2} [(k_{mx} + k_{hx})^2 + (k_{my} + \hat{k}_{hy})^2]} + \sqrt{\frac{1}{v(\mathbf{s}, z)^2} - \frac{1}{4\omega^2} [(k_{mx} - k_{hx})^2 + (k_{my} - \hat{k}_{hy})^2]} \right). \quad (\text{A-2})$$

Here,  $v(\mathbf{r}, z)$  and  $v(\mathbf{s}, z)$  are the velocities evaluated at depth  $z$  and source and receiver locations  $\mathbf{r}$  and  $\mathbf{s}$ , respectively. Lateral velocity variations can be accounted for by corrections such as the split-step expansion (Popovici, 1996). In the case of large variations, we use the PSPI technique (Gazdag and Sguazzero, 1984) in conjunction with a split-step correction (Kuehl and Sacchi, 2003). The spatial frequencies  $k_{mx}$  and  $k_{my}$  are the midpoint wavenumbers in the inline and crossline direction, respectively. In addition,  $k_{hx}$  is the inline offset wavenumber. The crossline offset wavenumber  $\hat{k}_{hy}$  is derived by a stationary-phase approximation (Biondi and Palacharla, 1996):

$$\hat{k}_{hy}(z) = k_{my} \frac{\sqrt{1/v_m^2 - 1/4\omega^2(k_{mx} + k_{hx})^2} - \sqrt{1/v_m^2 - 1/4\omega^2(k_{mx} - k_{hx})^2}}{\sqrt{1/v_m^2 - 1/4\omega^2(k_{mx} + k_{hx})^2} + \sqrt{1/v_m^2 - 1/4\omega^2(k_{mx} - k_{hx})^2}}. \quad (\text{A-3})$$

This formula is derived for constant velocities. But with proper implementation (e.g., PSPI), it can also image media with vertical and lateral velocity variations (Biondi and Palacharla, 1996). However, it is important to note that the stationary phase approximation entails a scaling factor that converts point sources to line sources (Biondi, 2003). We have omitted this factor here, keeping in mind that the data must be scaled to approximately simulate line sources.

At each depth, the wavefield is imaged at time zero by considering the following two steps. First, use the radial-trace transform to compute the image contribution of waves locally propagating with ray parameter  $p_{hx}$  (Sava et al., 2001). The relationship between offset ray parameter  $p_{hx}$ , frequency  $\omega$ , and offset wavenumber  $k_{hx}$  is given by

$$p_{hx} = \frac{k_{hx}}{\omega}. \quad (\text{A-4})$$

Second, sum the data along  $\omega$  in the radial-trace domain (Mosher and Foster, 2000).

The above algorithm produces CIGs in the ray-parameter domain. These image gathers can be transformed to the angle domain by the following expression (Prucha et al., 1999):

$$\sin(\theta) = \frac{v(\mathbf{m}, z) p_{hx}}{2 \cos(\phi)}, \quad (\text{A-5})$$

with the incident angle  $\theta$ , velocity  $v(\mathbf{m}, z)$  at the midpoint position  $\mathbf{m}$ , and apparent structural dip  $\phi$  along the inline direction. The formula is valid when the crossline dip is negligible. Fomel (2004) provides a generalization of the above relationship.

## REFERENCES

- Aki, K., and P. G. Richards, 1980, Quantitative seismology: W. H. Freeman & Co.
- Biondi, B., 2003, 3-D seismic imaging lecture notes: Stanford University.
- Biondi, B., and G. Palacharla, 1996, 3-D prestack migration of common-azimuth data: *Geophysics*, **61**, 1822–1832.
- Castagna, J. P., M. L. Batzle, and R. L. Eastwood, 1985, Relationship between compressional wave and shear wave velocities in clastic silicate rocks: *Geophysics*, **50**, 571–581.
- Clairbout, J. F., 2004, Image estimation by example: Geophysical soundings image construction: Multidimensional autoregression: Stanford Exploration Project, <http://sepwww.stanford.edu/sep/prof/>.
- de Bruin, C. G. M., C. P. A. Wapenaar, and A. J. Berkhout, 1990, Angle-dependent reflectivity by means of prestack migration: *Geophysics*, **55**, 1223–1234.
- Duquet, B., K. J. Marfurt, and J. A. Dellinger, 2000, Kirchhoff modeling, inversion for reflectivity, and subsurface illumination: *Geophysics*, **65**, 1195–1209.
- Ehinger, A., and P. Lailly, 1991, Prestack linearized inversion with a priori information: A step beyond prestack depth migration: 61st Annual International Meeting, SEG, Expanded Abstracts, 1289–1292.
- Fomel, S., 2004, Theory of 3D angle gathers in wave-equation imaging: 74th Annual International Meeting, SEG, Expanded Abstracts, 1053–1056.
- Fomel, S., and J. F. Clairbout, 2003, Multidimensional recursive filter preconditioning in geophysical estimation problems: *Geophysics*, **68**, 577–588.
- Gazdag, J., and P. Sguazzero, 1984, Migration of seismic data by phase shift plus interpolation: *Geophysics*, **49**, 124–131.
- Hanke, M., and P. C. Hansen, 1993, Regularization methods for large-scale problems: *Survey on Mathematics for Industry*, **49**, 253–315.
- Hansen, P., 1998, Rank-deficient and discrete ill-posed problems: Numerical aspects of linear inversion: SIAM Monograph on Mathematical Modeling and Computation.
- Hestenes, M., and E. Stiefel, 1952, Methods of conjugate gradients for solving linear systems: *National Bureau of Standards Journal of Research*, **49**, 403–436.
- Hu, I., G. T. Schuster, and P. A. Valasek, 2001, Poststack migration deconvolution: *Geophysics*, **66**, 1528–1537.
- Kuehl, H., 2003, Least-squares wave-equation migration/inversion: Ph.D. dissertation, University of Alberta.
- Kuehl, H., and M. D. Sacchi, 2002, Robust AVP estimation using least-squares wave-equation migration: 72nd Annual International Meeting, SEG, Expanded Abstracts, 281–284.
- , 2003, Least-squares wave-equation migration for AVP/AVA inversion: *Geophysics*, **68**, 262–273.
- Liu, B., M. Sacchi, and H. Kuehl, 2003, 2-D/3-D seismic wavefield reconstruction for AVA imaging: 73rd Annual International Meeting, SEG, Expanded Abstracts, 235–238.
- Mosher, C., and D. Foster, 2000, Common angle imaging conditions for prestack depth migration: 70th Annual International Meeting, SEG, Expanded Abstracts, 830–833.
- Mossop, G. D., and I. Shetsen, 1994, Geological atlas of the Western Canada Sedimentary Basin: Canadian Society of Petroleum Geologists and Alberta Research Council, Calgary, Alberta, [http://www.ags.gov.ab.ca/publications/atlas\\_www/atlas.shtml](http://www.ags.gov.ab.ca/publications/atlas_www/atlas.shtml).
- Nemeth, T., C. Wu, and G. T. Schuster, 1999, Least-squares migration of incomplete reflection data: *Geophysics*, **64**, 208–221.
- Popovici, A. M., 1996, Prestack migration by split-step DSR: *Geophysics*, **61**, 1412–1416.
- Prucha, M., and B. Biondi, 2002, Subsalt event regularization with steering filters: 72nd Annual International Meeting, SEG, Expanded Abstracts, 1176–1179.
- Prucha, M., B. Biondi, and W. Symes, 1999, Angle-domain common image gathers by wave-equation migration: 69th Annual International Meeting, SEG, Expanded Abstracts, 824–827.
- Ronen, S., D. Nichols, R. Bale, and R. Ferber, 1995, Dealiasing DMO: Good-pass, bad-pass, and unconstrained: 65th Annual International Meeting, SEG, Expanded Abstracts, 743–746.
- Saad, Y., 1991, Numerical methods for large eigenvalue problems: <http://www-users.cs.umn.edu/~saad/books.html>.
- Sava, P. C., and S. Fomel, 2003, Angle-domain common image gathers by wavefield continuation method: *Geophysics*, **68**, 1065–1074.
- Sava, P. C., B. Biondi, and S. Fomel, 2001, Amplitude-preserved common image gathers by wave-equation migration: 71st Annual International Meeting, SEG, Expanded Abstracts, 296–299.
- Stolt, R. H., and A. B. Weglein, 1985, Migration and inversion of seismic data: *Geophysics*, **50**, 2458–2472.
- Trad, D., T. Ulrych, and M. D. Sacchi, 2003, Latest views of the sparse Radon transform: *Geophysics*, **68**, 386–399.
- Wapenaar, C. P. A., A. J. Van Wijngaarden, W. Van Geloven, and T. Van der Leij, 1999, Apparent AVA effects of fine layering: *Geophysics*, **64**, 1939–1948.
- Xu, S., H. Chauris, G. Lambare, and M. S. Noble, 1998, Common angle image gather: A new strategy for imaging complex media: 68th Annual International Meeting, SEG, Expanded Abstracts, 1538–1541.